

# Rethinking Motion Deblurring Training: A Segmentation-Based Method for Simulating Non-Uniform Motion Blurred Images

Guillermo Carbajal, Patricia Vitoria, Pablo Musé, and José Lezama

**Abstract**—Successful training of end-to-end deep networks for real motion deblurring requires datasets of sharp/blurred image pairs that are realistic and diverse enough to achieve generalization to real blurred images. Obtaining such datasets remains a challenging task. In this paper, we first review the limitations of existing deblurring benchmark datasets from the perspective of generalization to blurry images in the wild. Secondly, we propose an efficient procedural methodology to generate sharp/blurred image pairs, based on a simple yet effective model for the formation of blurred images. This allows generating virtually unlimited realistic and diverse training pairs. We demonstrate the effectiveness of the proposed dataset by training existing deblurring architectures on the simulated pairs and evaluating them across four standard datasets of real blurred images. We observed superior generalization performance for the ultimate task of deblurring real motion-blurred photos of dynamic scenes when training with the proposed method.

**Index Terms**—Deblurring, non-uniform blur, motion blur, synthetic dataset, real images.

## I. INTRODUCTION

IN recent years, image restoration methods for tasks such as denoising or super-resolution have achieved outstanding progress, by leveraging the end-to-end training of deep neural networks. One aspect these tasks have in common is that simulating the degradation operator is relatively easy, so vast amounts of source/target image pairs can be generated for training. However, this is not the case for the task of single-image motion deblurring, where generating realistic training pairs has proven extremely laborious. Previous approaches have achieved impressive performance by leveraging high-speed cameras to generate sharp/blurred pairs [1]–[7], beamsplitter-based setups [8], or synthetically blurred images [9]. However, these datasets are naturally bounded in their diversity, making models trained on them limited in their ability to generalize to real “in the wild” motion-blurred images.

In this work we analyze the limitations of commonly used training datasets, such as GoPro [4], [5], REDS [10], DVD [2], RealBlur [8], and their generalization ability to wild real images. To overcome these limitations we propose a novel strategy to generate single-image, non-uniform motion deblurring training pairs, based on a model for the formation of blurred photos of dynamic scenes. The model of blurred image formation we propose retains the minimal elements

required to make data generation fast and virtually unlimited, while effectively inducing powerful generalization capabilities in neural networks trained on the generated data.

## A. Background

Motion blur is a major source of degradation in digital images. This effect occurs when the exposure time is large compared to the relative motion speed between the camera and the scene. As a result, the camera sensor at each pixel receives and accumulates light coming from different sources, producing different amounts of blur.

The complexity of the image formation process of real motion-blurred photos of dynamic scenes, and the unprecedented progress in learning approaches achieved by deep learning, have shifted attention from classic model-based methods toward supervised learning approaches. Recently, spectacular results have been reported by end-to-end deep neural networks [5], [12], [13], [15]–[19]. These supervised learning approaches are trained on pairs of sharp and motion-blurred images. Obtaining such pairs of images is not a trivial task and several approaches have been proposed. Here we focus on how to obtain such pairs.

One dominant approach is to select as ground truth the middle sharp image from a set of frames captured from a high-speed video of a dynamic scene, and the sequence average as the motion-blurred image [2], [6], [11]. In the case that source videos are captured in low-speed, in-between frames are interpolated prior to create the dataset. Methods trained on such datasets rely on the assumption that CNNs directly restore latent images without assuming any blur kernel model [5].

TABLE I  
PSNR PERFORMANCE IN THE WIDELY USED GoPro DATASET [11] IS NOT INDICATIVE OF PERFORMANCE IN REAL BLURRED PHOTOS. ALL METHODS WERE TRAINED WITH GoPro, EXCEPT ANA-SYN [9], WHICH WAS TRAINED ON OPEN IMAGES WITH SYNTHETIC UNIFORM BLUR.

Architecture	GoPro	Köhler	RealBlur
Ana-Syn [9]	28.01	<b>29.95</b>	<b>28.76</b>
DeepDeblur [5]	30.74	25.28	28.06
SRN [15]	30.72	27.18	28.56
DMPHN [16]	30.54	24.751	27.78
SDNet4 [16]	31.69	24.88	27.80
MiMO-UNet [12]	32.04	25.62	27.76
MiMO-UNet+ [12]	32.77	25.49	27.64
HiNet [13]	32.95	25.89	28.17
MPRNet [14]	<b>33.01</b>	26.57	28.70

G. Carbajal, P. Musé and J. Lezama are with the Department of Electrical Engineering, Universidad de la República, Uruguay. Patricia Vitoria is with the Image Processing Group, Universitat Pompeu Fabra, Spain.

Results on the GoPro dataset [11]

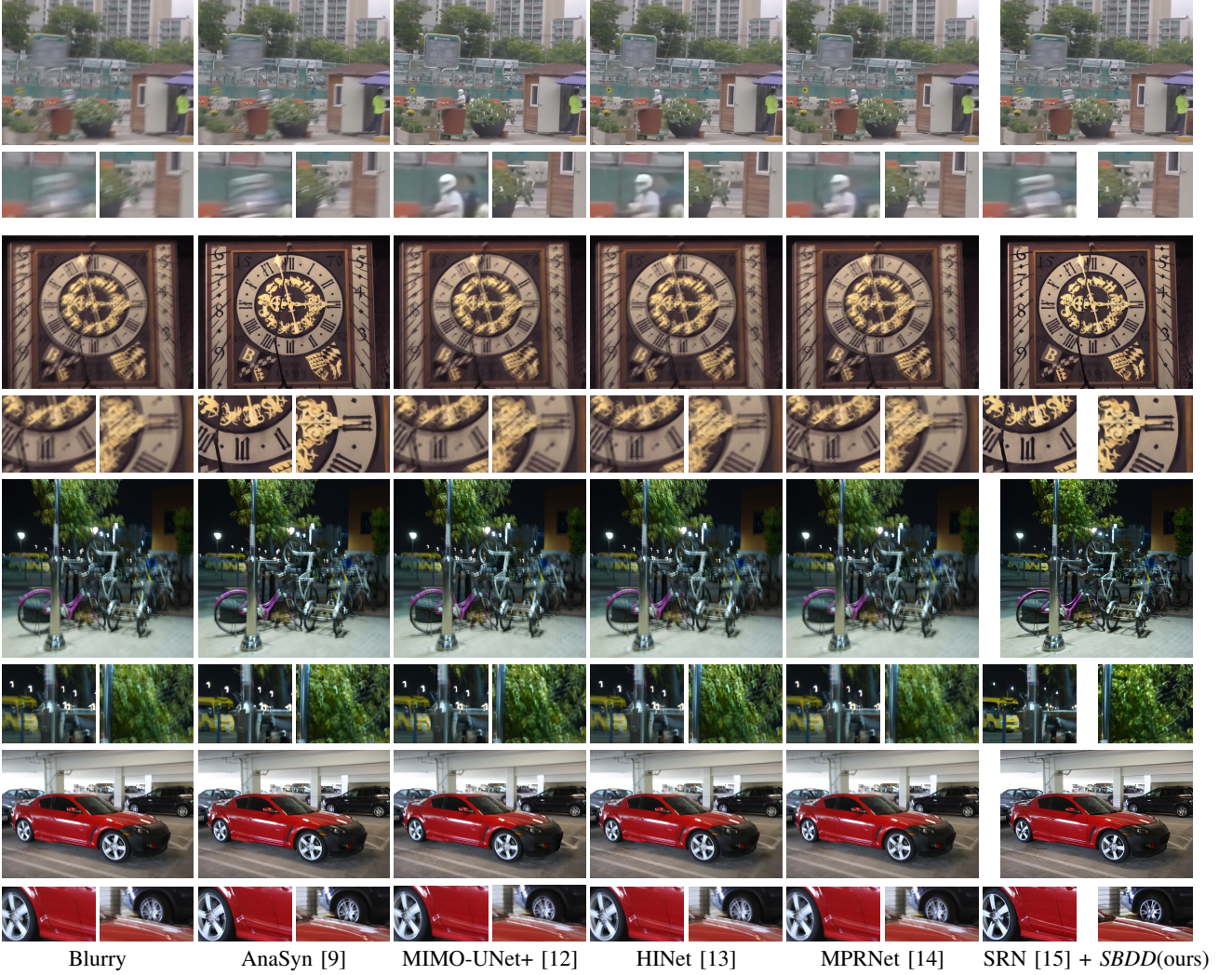


Fig. 1. State-of-the-art deblurring neural networks achieve spectacular restorations in the GoPro dataset [11] (top), but generalize poorly to real non-uniformly blurred images (bottom rows). We conjecture that this is due to a discrepancy of the underlying image model in these datasets, to that of actual blurred photographs of dynamic scenes. We propose a new model-based methodology for generating training pairs, that improves model performance in the ultimate task of deblurring real blurred images (right column).

However, we observed that such methods tend to produce inferior results when tested on images whose blur operators are not present in the training set. Indeed, as pointed out in [20], many deep-learning models degenerate to nearly an identity map when tested on out-of-domain blur operators. This issue, known as *kernel overfitting* [20], is particularly relevant when testing with real images, as shown quantitatively in Tab. I and depicted in Fig. 1. In the first row, when the test blurry image comes from the same dataset (GoPro) as they are trained with (MIMO-UNET+ [12], HiNet [13] and MPRNet [14]), state-of-the-art methods dramatically outperform the others. However, when tested on examples from three standard datasets of real images, the superiority of these methods does no longer stand.

Another strategy, presented recently by Rim *et al.* [8], is to use an image acquisition system that consists of two cameras built into a beamsplitter setup, that simultaneously captures pairs of blurred and sharp images using different exposure times. Using this method, the authors built RealBlur, the first

large-scale dataset of real-world blurred images suitable for training image deblurring deep networks.

A third commonly used strategy is to convolve sharp images with synthesized blur kernels. In this case, the real scene is typically assumed to be static and planar, and the blur operator is assumed to be uniform across the image. Using such data, the generalization ability of CNNs is superior among static and planar scenes [8], [9]. However, these approaches lead to unsatisfactory results when this hypothesis is not valid, i.e. when the underlying motion blur kernels vary rapidly in neighboring regions.

In the context of the approximation-generalization trade-off, current research has shown that CNNs excel in deblurring images with different amounts and types of blur within a dataset. A natural step forward is to also design methods with good out-of-distribution performance, capable to perform well on real world applications. In this work, we take a data-centric approach to closing this generalization gap.

## B. Contributions

We first present a review of the three common strategies for generating deblurring training pairs used in the literature: 1) averaging shots from high-speed cameras, 2) a dual-camera setup with different exposure configurations, and 3) synthetically blurred images by convolving a sharp image with a given kernel. Secondly, we propose a method that, based on the third strategy, is able to generate training pairs that induce powerful generalization in existing deblurring models, as evaluated on four standard datasets of real blurred images [8], [19], [21], [22]. Compared to existing approaches, our generation methodology takes into account multiple object motions in the scene and saturated pixels. Experimentally, we found that these two additional elements are crucial for obtaining good generalization to real images, as they allow the network to see smoothly varying motion blur kernels within objects, and at the same time, to learn to restore patches where multiple motion blurs and saturation coexist. The proposed dataset generation procedure is simple, effective, and allows to distill the impact in the network's performance of modeling aspects like  $\gamma$ -correction, kernel size, non-uniformity, and pixel saturation.

## II. EXISTING DEBLURRING DATASET GENERATION STRATEGIES

### A. High Speed Camera-based Generation

High-speed camera-based datasets produce blurred images by averaging a set of consecutive sharp images from a high-speed video [1]–[5], [7], [10]. The integrated signal is then transformed into pixel value by a nonlinear CRF (Camera Response Function). Thus, the blurring process is modeled as follows:

$$\mathbf{v} = g\left(\frac{1}{T} \int_{t=0}^T \tilde{\mathbf{u}}(t) dt\right) \simeq g\left(\frac{1}{M} \sum_{i=0}^{M-1} \tilde{\mathbf{u}}[i]\right), \quad (1)$$

where  $T$  and  $\tilde{\mathbf{u}}(t)$  denote the exposure time and the sensor signal of a sharp image at time  $t$ , respectively. Similarly,  $M$  and  $\tilde{\mathbf{u}}[i]$  are the number of sampled frames and the  $i$ -th sharp frame signal captured during the exposure time, respectively. The function  $g$  is the CRF that maps the average of scene irradiances  $\tilde{\mathbf{u}}[i]$  into an observed intensity image. The sharp image in each sharp-blurry pair is typically chosen to be the central frame of the sequence that is averaged.

It has been shown that nonlinear CRFs affect the blur in the image [23], for example, causing a spatially invariant blur to behave as a spatially varying blur. While a pre-calibrated CRF is undoubtedly the optimal solution, the CRF may not always be available and may also be scene dependent, when the camera is in “auto” mode. A common practice is to approximate the CRF as a gamma curve with  $\gamma = 2.2$ ,

$$g(x) = x^{1/\gamma}, \quad (2)$$

as it is an approximated average of known CRFs [23]. Thus, by correcting the gamma function, the latent frame signal  $\tilde{\mathbf{u}}[i]$  is obtained from the observed image  $\mathbf{u}[i]$ . The corresponding blur image  $\mathbf{v}$  is then synthesized using Eq. (1). It is worth noticing

that the GoPro dataset [11] has two versions, one that assumes a linear CRF ( $\gamma=1$ ) and another that applies  $\gamma$ -correction with  $\gamma = 2.2$ . We call the latter GoPro( $\gamma$ ). REDS [10] accounts for  $\gamma$ -correction, while DVD [2] does not.

The quantity and type of blur operators modeled by these methods are limited by the number and variety of captured sequences. Also, the specific recording devices used for each dataset may undermine the generalization of the algorithms to other cameras. Moreover, contrary to real kernels, the implicit kernels are prone to be discrete since cameras have a duty cycle that prevents continuous acquisition. This produces, in fast-moving objects, a well-known ghosting effect that is far from what is observed in real motion-blurred images. While this artifact may be reduced by using cameras with even higher frame rates, the captured “sharp” frames may not be suitable due to their low SNR. Also, as the middle frame of the sequence is considered the “sharp” frame, some moving objects may appear only in the blurry frame. REDS [10] tries to reduce ghosting while keeping the noise level reasonable by means of inter-frame interpolation.

### B. Real Blurred Images Datasets

Simultaneously generating pairs of real blurred images and corresponding sharp ones is extremely challenging and requires special hardware setups. To the best of our knowledge, there are only two datasets with real ground-truth sharp/blurred pairs available: Köhler [21] and RealBlur [4].

The Köhler *benchmark dataset* [21] is composed of 48 blurry images taken by a high-precision robot, capturing 4 posters placed at a distance of 62 cm to the camera. The trajectory followed by the robot during the blurry image acquisition corresponds to that of 12 human shakes previously recorded. For each blurry image, 167 images were taken as ground-truth candidates, by playing back the trajectory in 167 steps and taking one sharp photograph per step. The main drawbacks of this dataset are the planar scene, its limitation to camera motion and its small size.

RealBlur [8] is a dataset collected in low-light environments with an image acquisition system that simultaneously captures geometrically aligned pairs of blurred and sharp images. The dataset consists of two subsets sharing the same image contents, one generated from camera raw images and the other from JPEG images processed by the camera ISP. In both cases, the captured images were also post-processed for noise reduction as well as for geometric and photometric alignment. Despite this carefully engineered procedure for generating real sharp/blur pairs, training on this dataset poses the risk of overfitting to the specific capturing device and the considered transformations.

Additionally, two standard datasets of real blurred images, but without ground truth sharp correspondences, are proposed in Lai *et al.* [22] and Zhang *et al.* [19]. The former introduced a dataset composed of 100 images from various types of scenes acquired with different cameras. The latter introduced the Real-World Blurred Image dataset (RWBI), which includes diverse blurry images recorded using several hand-held devices. The dataset contains several sequences with a total of over 3000 images.

### C. Synthetic kernel-based Datasets

Kernel-based methods generate blurry/sharp image pairs by convolving sharp images with synthetic blur kernels. We first review kernel simulation methods that have been used to build training datasets and then how to use them to generate motion-blurred images.

**Kernels Simulation** Chakrabarty [24] generates synthetic motion kernels by randomly sampling six points in a limited size grid, fitting a spline through the points, and setting the kernel values at each pixel on this spline to a value sampled from a narrow Gaussian. An adaptation of this method has been applied by Kaufman *et al.* [9].

To generate random motion kernels [25] propose a camera-shake kernel generator based on physiological hand tremor data [26]. The shape and size of the motion blur kernel are controlled by a single parameter, the exposure time. Schmidt *et al.* [27] propose to sample random 3D trajectories using a simple linear motion model and then to project and rasterize the obtained trajectories to random square kernels of varying sizes. This method was later used by RealBlur [8] and Lai *et al.* [22] to synthesize uniformly blurry images. Lai *et al.* [22] also incorporate 6D camera trajectories by using a cellphone with inertial sensors (gyroscope and accelerometer) and construct a collection of spatially varying blur kernels by assuming constant depth scenes.

To deal with the inherent phase ambiguity [24] proposes a “canonical” translation by centering them so that each kernel’s center of mass is located at the center of the window. This strategy was also confirmed as useful by [8].

**Blurry image generation** Most kernel-based methods in the literature use a blur kernel to generate uniformly blurred images according to the degradation model

$$\mathbf{v} = \mathbf{k} * \mathbf{u} + \mathbf{n}, \quad (3)$$

where  $\mathbf{u}$  is the latent sharp image,  $\mathbf{k}$  the blurring kernel and  $\mathbf{n}$  is typically white, Gaussian noise. Chakrabarty [24] obtained sharp frames from Pascal VOC 2012; Kaufmann *et al.* [9] used random generated crops of size  $512 \times 512$  extracted from the Open Image Dataset [28], Rim *et al.* [8] generated  $256 \times 256$  crops from BSD500 [29], and Schuler *et al.* [30] used  $256 \times 256$  random crops from ImageNet [31].

Lai *et al.* [22] examined the performance consistency between real and synthetic images by collecting 25 sharp images from the internet as ground truth and synthesizing 100 non-uniformly and 100 uniformly blurred images. To synthesize non-uniformly blurred images, a homography-based model for camera shakes and the recorded trajectories were used. Note that this model assumes a planar scene and does not account for the more realistic scenario of different moving objects. To synthetically generate saturated images in both datasets, the intensity range of the latent image was stretched from  $[0, 1]$  to  $[-0.1, 1.8]$ , convolved with the blur kernels, and then clipped to the range  $[0, 1]$ .

While methods trained with uniformly-blurred images show remarkable generalization properties when (3) holds, they cannot restore patches with objects’ boundaries where multiple

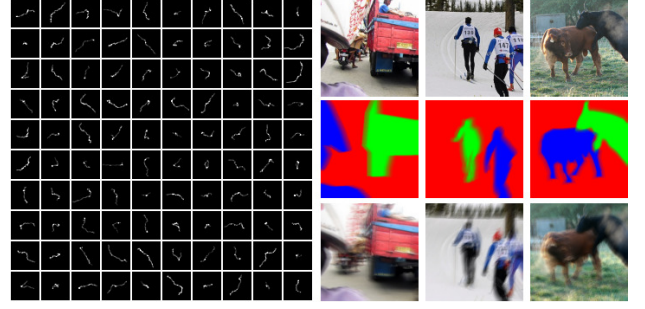


Fig. 2. Examples of synthetic blurred images generated by the proposed procedure. From left to right: camera-shake motion kernels from physiological tremor model [26]; image from the COCO dataset [32]; corresponding segmentation masks; resulting motion blurred image, obtained by convolving each region in the image with a different blur kernel.

motion blurs coexist. In this work, we propose to extend this procedure to account for the case of saturated and non-uniformly motion-blurred images.

### III. SEGMENTATION-BASED GENERATION OF MOTION BLUR TRAINING PAIRS

In this section, we present a simple yet effective method to generate blurry/sharp image pairs accounting for non-uniform motion blur, that overcomes several limitations of the existing datasets. Using this procedure, we generate a new dataset, called *SBDD* (Segmentation-Based Deblurring Dataset).<sup>1</sup> In Sec. IV, we show how the proposed *SBDD* is capable of boosting the generalization capacity of existing end-to-end architectures in the real motion blur scenario.

#### A. The Non-Uniform Motion Blur Degradation Model

Non-uniform motion blur can be modeled as the local per-pixel convolution of a sharp image with a spatially varying filter, the *motion blur field*.

Given a sharp image  $\mathbf{u}$  of size  $H \times W$ , and a set of per-pixel blur kernels  $\mathbf{k}_i$  of size  $K \times K$ , the observed blurry image  $\mathbf{v}$  is generated as

$$v_i = \langle \mathbf{u}_{nn(i)}, \mathbf{k}_i \rangle + n_i, \quad (4)$$

where  $\mathbf{u}_{nn(i)}$  is a window of size  $K \times K$  around pixel  $i$  in image  $\mathbf{u}$ , and  $n_i$  is additive noise. We assume non-negative kernels (no negative light) of area one (conservation of energy).

By considering the sensor saturation and gamma correction, the model becomes

$$v_i = R(\langle \mathbf{u}_{nn(i)}^\gamma, \mathbf{k}_i \rangle + n_i)^\frac{1}{\gamma}, \quad (5)$$

where  $\gamma$  stands for the gamma correction coefficient and  $R(\cdot)$  is the pixel saturation operator that clips image values  $v_i$  which are larger than 1.

Simulating realistic blurry images with pixel-wise non-uniform kernels is extremely hard. On the other hand, assuming uniform blur across the image is unrealistic in most cases, as illustrated in Fig. 6.

<sup>1</sup>Dataset and trained models are publicly available at <https://github.com/GuillermoCarbajal/SegmentationBasedDeblurringDataset>

An intermediate approach that allows to extend the capacity of deblurring networks to deal with non-uniform blur is to assume piece-wise constant blur:

$$v_i = R(\langle \mathbf{u}_{nn(i)}^\gamma, \sum_{b=1}^B \mathbf{k}^b m_i^b \rangle + n_i)^{\frac{1}{\gamma}}, \quad (6)$$

where  $B$  is the number of uniform blur regions,  $m_i^b$  is the mask that defines region  $b$ , and  $\mathbf{k}^b$  is the kernel associated with that region.

### B. Synthetic Dataset Generation

We generate a set of blurry/sharp image pairs using the degradation model defined by (6), and the camera-shake kernel generator [25], [26]. Sharp images and corresponding segmentation masks are obtained directly from the COCO [32] and the ADE20K [33] semantic segmentation datasets. Since persons and license plates are blurry in the currently available ADE20K dataset, COCO images are better for generating blurry/sharp pairs. However, COCO has no segmented classes related to different lighting conditions, which is handy to simulate more realistic saturated images. Therefore, we used both datasets, COCO to build a set of dynamic scenes blurry images, and ADE20K to generate another set designed to include more diverse lighting conditions. We follow the same procedure to build both sets, the only difference is in the data augmentation step. We first present the general procedure, then we describe how we generated the Dynamic Scenes Set and the Varying Illumination Set.

1) *Procedure*: Given a random sharp image  $\mathbf{u}$ , and corresponding objects segmentation masks, we apply separate random kernels to the background and to each segmented object. To ensure a soft transition between regions, we fuse neighboring segmentations by applying the corresponding kernel to the objects' masks in (6). The goal of this procedure is to provide the network with examples of patches containing multiple motion blurs while avoiding hard transition artifacts at the objects' boundaries.

Before convolving with each corresponding kernel, we apply the inverse  $\gamma$ -correction to the sharp image and perform an illumination augmentation step, described below, to account for sensor saturation and different lighting conditions. Then, we convolve each segment with a random kernel, and fuse them weighted by the masks. Finally, we apply  $\gamma$ -correction to the resulting image. By following this procedure, we generated two sets: the *Dynamic Scenes* and *Varying Illumination* sets.

2) *Dynamic Scenes Set*: We generated blurry images from 10,000 images of the COCO dataset [32] having at least one moving object segmented. We chose three COCO super-categories as moving objects (persons, vehicles and animals), to avoid simulating different blur for typically non-moving objects (e.g. trees). We applied the procedure described above with a simple data augmentation step to account for different exposures of natural images. First, sharp images are converted to *hsv* color space, and the histogram is transformed by multiplying the *v*-channel by a random value between  $[0.5, 1.5]$ . The transformed image is converted back to the *rgb* space, and the

blurry image is generated as described in Sec. III-B1. Finally, the blurry image is clipped to the  $[0, 1]$  range. A maximum of two segmented objects with a minimum size of 400 pixels are considered for each image. Results in Sec. IV show that the obtained methods generalize remarkably well to multiple object classes. The pseudo-code of the generation procedure is presented in Algorithm 1.

---

#### Algorithm 1 Dataset Generation

---

##### Input

$\mathbf{u}, \{\mathbf{k}\}, \gamma$  ▷ Sharp Image, dataset of kernels and  $\gamma$  factor

**procedure** BLURIMAGE( $\mathbf{u}, \{\mathbf{k}\}, \gamma$ )

$\mathbf{k}_u, \mathbf{m}_u = [], []$  ▷ List of kernels and masks initialization

$\mathbf{k}_u.append(Random(\{\mathbf{k}\}))$  ▷ Background kernel added to the list

$\mathbf{m}_u.append(ones(size(\mathbf{u})))$  ▷ Background mask initialization

**for**  $\mathbf{m} \in SegmentedObjectMasks(\mathbf{u})$  **do**

$\mathbf{k} = Random(\{\mathbf{k}\})$  ▷ Object kernel

$\mathbf{m} = \mathbf{m} * \mathbf{k}$  ▷ Smooth mask

$\mathbf{m}_u[0] = \mathbf{m}_u[0] - \mathbf{m}$  ▷ Update background mask

$\mathbf{k}_u.append(\mathbf{k})$  ;  $\mathbf{m}_u.append(\mathbf{m})$

**end for**

$\mathbf{u}_{ph} = \mathbf{u}^\gamma$  ▷ Convert to photons

$\mathbf{u}_{ph} = illum\_augment(\mathbf{u}_{ph})$  ▷ cf. Section III.B.2

$\mathbf{v}_{ph} = zeros(size(\mathbf{u}))$  ▷ Initialize blurry image

**for**  $\mathbf{k}, \mathbf{m} \in \mathbf{k}_u, \mathbf{m}_u$  **do**

$\mathbf{v}_{ph} = \mathbf{v}_{ph} + \mathbf{m}(\mathbf{k} * \mathbf{u}_{ph})$

**end for**

$\mathbf{u} = \mathbf{u}_{ph}^{1/\gamma}$ ; ▷ sharp is converted-back to pixels

$\mathbf{v} = \mathbf{v}_{ph}^{1/\gamma}$  ▷ blurry is converted-back to pixels

**return**  $\mathbf{u}, \mathbf{v}$  ▷ Blurred-Sharp pairs

**end procedure**

---

3) *Varying Illumination Set*: Among the ADE20K classes, 18 of them are related to illumination objects or artifacts, (e.g. bulb, ceiling spotlight, spotlight, pendant lamp). We filtered the ADE20K dataset by keeping those images that contain objects of these classes, and for which the area of high intensity pixels value ( $> 250$ ) does not exceed 0.1% of the image area. These regions are used to define the saturation mask for each image. We also discarded images containing persons, as these were blurred out in the latest version of the ADE20K dataset. We used a subset of 1,621 original images. Applying the following data augmentation procedure, we synthesized several blurry images from each original sharp image. First, we convert sharp images to the *hsv* color space, then the histograms of the segmented and non-segmented regions are transformed separately. The *v*-channel of non-saturated pixels is multiplied by  $(0.25 + l)$ , where  $l$  is a random value drawn from the interval  $[0, 0.75]$ . Illumination in non-saturated pixels is kept constant or reduced. The *v*-channel of the segmented pixels is multiplied by  $(0.25 + l + s)$ , where  $s$  is a random value drawn from the interval  $[0, 1]$ . Then, we convert the transformed image back to the *rgb* color space and generate the blurry image as described in Sec. III-B1. Finally, we clipped the blurry image to the  $[0, 1]$  range. We simulated

eight blurry/sharp pairs for each original image under different illumination conditions. Fig. 3 shows some examples.



Fig. 3. Different blurry/sharp pairs are generated multiplying the  $v$ -channel of segmented and non-segmented regions by different factors, to simulate saturation and different lighting conditions.

### C. Training Set Details

In total, our *SBDD* dataset consists of: (i) 10,000 pairs belonging to the *Dynamic Scenes* Set, each blurry image was generated with kernels on patches of size  $65 \times 65$ ; (ii) 25,936 pairs as part of the *Varying Illumination* Set, half of them using kernels simulated on patches of size  $33 \times 33$ ; the other half on patches of size  $65 \times 65$ . This makes a total of 35,936 sharp/blurred pairs generated from 10,000 original sharp images from COCO and 1,621 from ADE20K. We generate a similar dataset with  $\gamma = 2.2$  that we term *SBDD*( $\gamma$ ). Experimentally, we observed good performance without adding synthetic noise. We refer the reader to the Appendix for experiments with added noise.

### D. Limitations of the Generated Dataset

Our model assumes smooth transitions between the objects and the background, which is unrealistic. While more realistic models for transition do exist [34], these methods require prior knowledge of the scene’s depth, adding complexity to the simulation procedure. Because this boundary effect is very local, a simple smooth transition is sufficient in practice.

TABLE II

GENERALIZATION PERFORMANCE TO REAL BLURRED IMAGES OF DEEP DEBLURRING MODELS TRAINED WITH DIFFERENT DATASETS. SINCE KÖHLER USES A LINEAR RESPONSE FUNCTION, WE GENERATE A VERSION OF OUR DATASET WITH  $\gamma = 1$  THAT HIGHLIGHTS THE IMPORTANCE OF  $\gamma$ -CORRECTION. THE BEST CROSS-DATASET PERFORMANCE IS INDICATED IN BOLD.

Model + Training Set	Test Sets	
	RealBlur	Köhler
SRN + GoPro	28.56/ 0.867	27.18/ 0.787
SRN + GoPro ( $\gamma$ )	28.55/ 0.863	26.38/ 0.771
SRN + REDS	28.95/ 0.868	25.46/ 0.741
SRN + BSD-B	28.68/ 0.868	28.07/ 0.826
SRN + RealBlur	30.99/ 0.899	26.57/ 0.799
SRN + <i>SBDD</i>	29.64/ 0.897	<b>29.01/ 0.828</b>
SRN + <i>SBDD</i> ( $\gamma$ )	<b>29.94/ 0.898</b>	27.70/ 0.812
DeepDeblur + GoPro ( $\gamma$ )	28.06/ 0.855	25.28/ 0.743
DeepDeblur + REDS	27.96/ 0.860	26.03/ 0.763
DeepDeblur + <i>SBDD</i> ( $\gamma$ )	<b>29.03 / 0.878</b>	<b>27.23/ 0.802</b>

Moreover, as the loss term optimizes the result to resemble the ground truth, sharp-image prior knowledge is introduced during training, which may help restore occluded regions or regions where the blur kernel is complex.

Blur due to camera movements, such as rotations, zoom-in, or zoom-out, is not explicitly described by our model. However, experimentally we notice it is possible to deblur images affected by those movements. We attribute this behavior, in part, to the fact that the convolution is a local operation that manages to locally approximate global motions. Nonetheless, it is worth pointing out that the proposed model performs better in those cases than assuming a uniform blur across the image.

## IV. EXPERIMENTS

The experiments aim to show that the procedural synthesis of diverse and realistic blurry/sharp pairs is a promising alternative for generating training data, compared to high-speed camera-based synthesis [1]–[7], complex hardware setups [8], or using synthetic uniform blur kernels [9], and leads to better generalization performance. Here again, given the difficulty of constructing true blurry/sharp pairs for evaluation, we argue in favor of visual inspection of real deblurred images as the ultimate verdict.

As shown in Tab. I, recent motion deblurring methods report their performance on the GoPro dataset. Although major progress has been made in this challenging dataset, this improvement is not necessarily extensive to actual real blurry images. For example, note that MPRNet [14] is more than 2dB better than SRN [15] in the GoPro test set, but its performance is worst in the theoretically much simpler Köhler test set. This could be pointing to an overfitting issue, due to the greater capacity of MPRNet. Thus, in order to show the generalization capabilities that induces our dataset, in our experiments we focus on two standard network architectures: SRN [15] and DeepDeblur [5], both for being less prone to overfit and computationally efficient. Here we do not intend to compare both networks but to show that the generalization performance in real blurry images of both networks is better when trained with the proposed *SBDD* dataset instead of their default training sets.

We trained SRN for 300 epochs and DeepDeblur for 200 epochs with the *SBDD* and *SBDD*( $\gamma$ ) datasets using the same hyperparameters as in [15] and [5]. We used the code of [8] for quantitative evaluations.

### A. On the Generalization to Real Blurred Images

Quantitative results of our study of dataset generalization to real images are presented in Tab. II. We show the result of training two efficient architectures on different standard datasets, and their performance on two datasets with real blurred images: Realblur [8], and Köhler [21]<sup>2</sup>. In the case of

<sup>2</sup>Since the Köhler dataset used a linear  $\gamma$  function, better results are obtained by datasets that do not account for  $\gamma$ -correction.

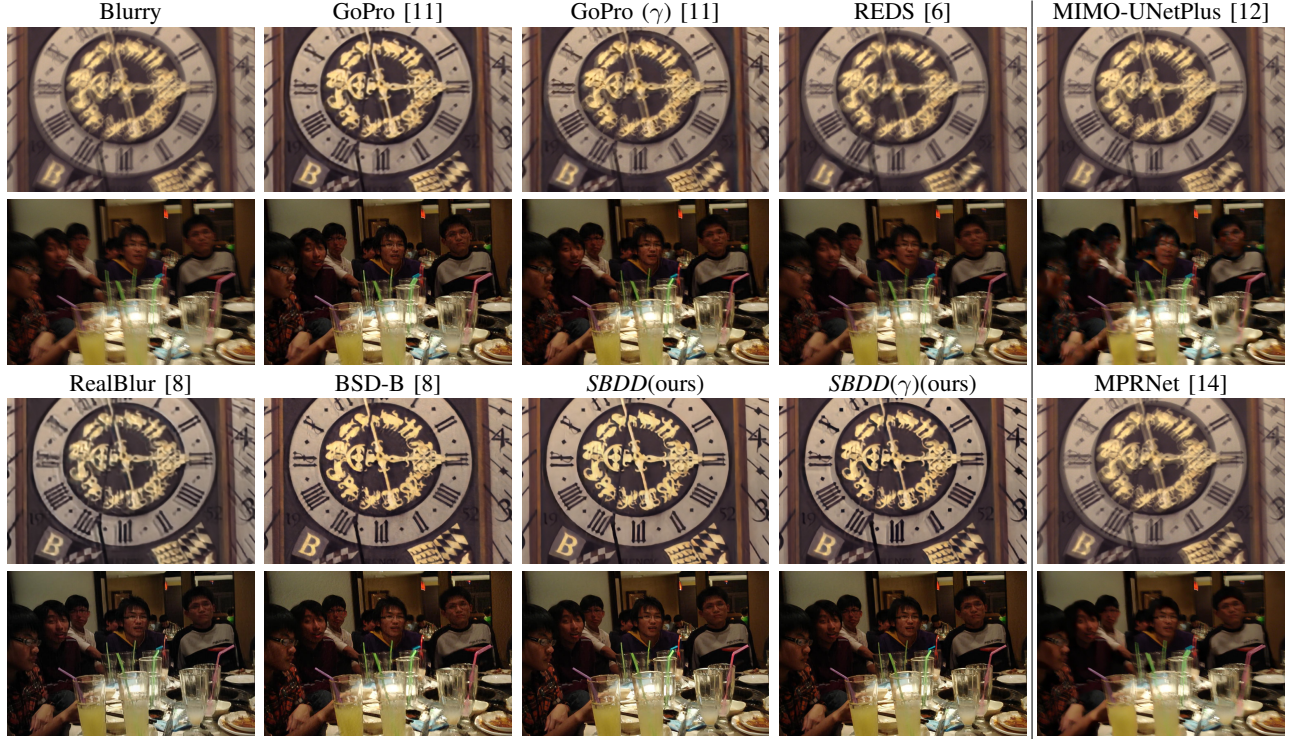


Fig. 4. In real blurred images, datasets generated using synthesized blur kernels (BSD-B [8]) and the proposed *SBDD*, *SBDD*( $\gamma$ ) produce better results than averaging high-speed camera frames (GoPro, GoPro( $\gamma$ ), REDS), and RealBlur. We trained SRN [15] on different datasets (specified above each example) and evaluated on: **1<sup>st</sup> and 3<sup>rd</sup> row**: image from Köhler dataset. **2<sup>nd</sup> and 4<sup>th</sup> row**: image from Lai [22]. **Right column**: For reference, we included results from very recently published deep deblurring methods.

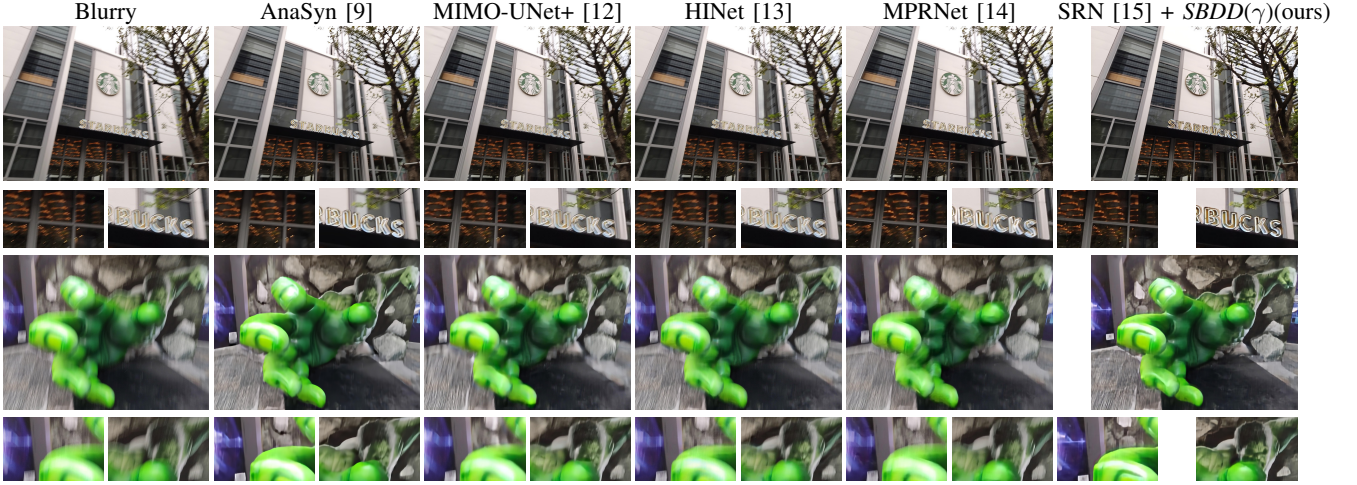


Fig. 5. Comparison to recent deep deblur methods in the Real-World Blurred Image (RWBI) dataset [19] of images with real blur. The proposed methodology produces better restorations while being based on the simpler SRN architecture. More results in the Appendix.

RealBlur, training with the proposed *SBDD* datasets produces the best results among the cross-dataset evaluations<sup>3</sup>.

Qualitative results reinforcing these findings are shown in Fig. 4 for the SRN architecture [15], and results for DeepDeblur [5] are presented in the Appendix. In both cases, training on the proposed *SBDD* dataset induces better generalization to real blurred images. We also include the comparison to state-of-the-art models, to show that the simpler SRN and

<sup>3</sup>Although RealBlur uses a nonlinear CRF, the gap between training with or without the  $\gamma$ -corrected dataset is smaller because of the photometric transformation applied in the dataset as a post-processing step.

DeepDeblur networks achieve better real image deblurring than more complex recent architectures. In Fig. 16 we present results on real blurred images from the RWBI dataset [19]. Further qualitative results are presented in the Appendix.

#### B. A Single Training for Different CRFs

Results shown in Tab. II highlight the importance of  $\gamma$ -correction in deblurring results. In most practical cases, the CRF used by the acquisition device is unknown, and neither is handy to train a model for each possible  $\gamma$ -correction curve. We propose to restore the image in the photons' space by



Fig. 6. Evaluation of synthetic blur datasets in a non-uniformly blurred image from GoPro [11]. Methods ordered according to performance (PSNR/ SSIM) for this image: Ana-Syn (27.28/0.850), BSD-B (30.71/ 0.900), SRN+SBDD (31.42/ 0.920). Note that training with databases that simulate uniform blur performs well, except at the boundaries of moving objects. Training SRN with the proposed *SBDD* dataset allows to better restore the boundaries of moving objects, as the network learns from patches where multiple motion blurs coexist.

inverting the  $\gamma$ -correction before feeding the network with the blurry image. Then, the output of the network is  $\gamma$ -corrected before computing the *loss*. In the Appendix, we show quantitatively for several synthetic and real datasets that a model trained with *SBDD*( $\gamma$ ) in the space of photons can be used to effectively restore images under different CRFs by simply changing the  $\gamma$ -factor in inference time.

### C. Uniform vs. Non-Uniform Synthetic Blur

One of the main features of our data generation method is the modeling of non-uniform blur, where different motion blurs are applied to different objects from segmented scenes. In the following experiment, we validate this approach and compare its performance to the one obtained when training with uniformly blurred images, in the task of deblurring real blurred images of dynamic scenes. We benchmark Analysis-Synthesis [9], which was trained with uniformly blurred images from Open Images, SRN trained with uniformly blurred images from BSD-B [8], and SRN trained with the proposed *SBDD*. We evaluate quantitatively on GoPro [11], Lai non-uniform [22], and RealBlur datasets [8]. Quantitative results presented in Tab. III show that training with non-uniform blur improves generalization. Fig. 6 shows qualitatively how our approach, compared to approaches synthesizing uniform blur, achieves much higher performance when deblurring small moving objects in a dynamic scene from the GoPro dataset.

TABLE III

CROSS-DATASET EVALUATION TO QUANTIFY THE CAPACITY OF METHODS TO DEAL WITH NON-UNIFORM BLUR. SRN TRAINED WITH A UNIFORM BLUR DATASET (BSD-B) CAN DEAL WITH SOME NON-UNIFORM BLURRY IMAGES. ANA-SYN EXCELS WITH UNIFORM BLURRY IMAGES BUT STRUGGLES WITH NON-UNIFORM BLURRY IMAGES.

Arch + Training Sets	Test Sets		
	GoPro	Lai (non.u )	RealBlur
SRN + GoPro (non-u.)	-	21.25/ 0.668	28.56/ 0.867
SRN + BSD-B (u.)	28.90/ 0.874	22.63/ 0.738	28.68/ 0.868
SRN + <i>SBDD</i> (non-u.)	<b>29.61/ 0.895</b>	<b>22.83/ 0.740</b>	<b>29.65/ 0.897</b>
Ana-Syn + Open Images (u.)	28.02/ 0.864	21.45/ 0.695	28.78/ 0.864

### D. Modeling Saturated Pixels

Photographs taken in low-light conditions typically contain blurred saturated pixels when a light source is present in the

image. By modeling saturated pixels in our image formation model, as explained in Sec. III-B3, neural networks trained with the proposed *SBDD* dataset can effectively handle challenging saturation conditions. This can be seen in particular in the second example in Fig. 1, and in two other extreme examples in Fig. 7.

## V. CONCLUSIONS

Deep deblurring networks have shown an impressive capacity to restore image information after heavy degradation from motion blur. However, creating a dataset of blurred and corresponding sharp images is an extremely difficult problem, so most modern methods are trained on datasets of simulated blurred images from high-speed cameras, non-trivial setups, or synthetic blur. In this paper, we first observed that modern deblurring networks tend to overfit to the particularities of training datasets, and their in-distribution performance is not indicative of real deblurring ability in out-of-distribution blurred images. Secondly, we propose a novel methodology for generating training pairs, by simulating motion blur (either uniform or non-uniform) under different conditions (saturated or unsaturated scenes). As a result, an arbitrarily large training set can be generated, allowing a significant increase in the generalization performance of existing deblurring networks, particularly for real motion-blurred photographs.



Fig. 7. Comparison of saturated pixels restoration by methods trained on synthetically blurred datasets, in low-light images from the RealBlur dataset [8]. Our image formation model accounts for pixel saturation, and the resulting deblurring network can successfully handle it.

## REFERENCES

- [1] A. Agrawal and R. Raskar, "Optimal single image capture for motion deblurring," in *2009 IEEE Conference on Computer Vision and Pattern Recognition*. IEEE, 2009, pp. 2560–2567.
- [2] S. Su, M. Delbracio, J. Wang, G. Sapiro, W. Heidrich, and O. Wang, "Deep video deblurring for hand-held cameras," in *Proceedings of the IEEE Conference on Computer Vision and Pattern Recognition*, 2017, pp. 1279–1288.
- [3] P. Wieselhollek, M. Hirsch, B. Scholkopf, and H. Lensch, "Learning blind motion deblurring," in *Proceedings of the IEEE International Conference on Computer Vision*, 2017, pp. 231–240.
- [4] T. H. Kim, S. Nah, and K. M. Lee, "Dynamic video deblurring using a locally adaptive blur model," *IEEE transactions on pattern analysis and machine intelligence*, vol. 40, no. 10, pp. 2374–2387, 2017.
- [5] S. Nah, T. Hyun Kim, and K. Mu Lee, "Deep multi-scale convolutional neural network for dynamic scene deblurring," in *Proceedings of the IEEE conference on computer vision and pattern recognition*, 2017, pp. 3883–3891.
- [6] S. Nah, S. Baik, S. Hong, G. Moon, S. Son, R. Timofte, and K. Mu Lee, "Ntire 2019 challenge on video deblurring and super-resolution: Dataset and study," in *Proceedings of the IEEE/CVF Conference on Computer Vision and Pattern Recognition Workshops*, 2019, pp. 0–0.
- [7] Z. Shen, W. Wang, X. Lu, J. Shen, H. Ling, T. Xu, and L. Shao, "Human-aware motion deblurring," in *Proceedings of the IEEE/CVF International Conference on Computer Vision*, 2019, pp. 5572–5581.
- [8] J. Rim, H. Lee, J. Won, and S. Cho, "Real-world blur dataset for learning and benchmarking deblurring algorithms," in *Proceedings of the European Conference on Computer Vision (ECCV)*, 2020.
- [9] A. Kaufman and R. Fattal, "Deblurring using analysis-synthesis networks pair," in *Proceedings of the IEEE/CVF Conference on Computer Vision and Pattern Recognition*, 2020, pp. 5811–5820.
- [10] S. Nah, S. Baik, S. Hong, G. Moon, S. Son, R. Timofte, and K. M. Lee, "Ntire 2019 challenge on video deblurring and super-resolution: Dataset and study," in *CVPR Workshops*, June 2019.
- [11] S. Nah, T. H. Kim, and K. M. Lee, "Deep multi-scale convolutional neural network for dynamic scene deblurring," in *The IEEE Conference on Computer Vision and Pattern Recognition (CVPR)*, July 2017.
- [12] S.-J. Cho, S.-W. Ji, J.-P. Hong, S.-W. Jung, and S.-J. Ko, "Rethinking coarse-to-fine approach in single image deblurring," in *Proceedings of the IEEE/CVF International Conference on Computer Vision*, 2021, pp. 4641–4650.
- [13] L. Chen, X. Lu, J. Zhang, X. Chu, and C. Chen, "Hinet: Half instance normalization network for image restoration," in *Proceedings of the IEEE/CVF Conference on Computer Vision and Pattern Recognition (CVPR) Workshops*, June 2021, pp. 182–192.
- [14] S. W. Zamir, A. Arora, S. Khan, M. Hayat, F. S. Khan, M.-H. Yang, and L. Shao, "Multi-stage progressive image restoration," in *Proceedings of the IEEE/CVF Conference on Computer Vision and Pattern Recognition*, 2021, pp. 14 821–14 831.
- [15] X. Tao, H. Gao, X. Shen, J. Wang, and J. Jia, "Scale-recurrent network for deep image deblurring," in *Proceedings of the IEEE Conference on Computer Vision and Pattern Recognition*, 2018.
- [16] H. Zhang, Y. Dai, H. Li, and P. Koniusz, "Deep stacked hierarchical multi-patch network for image deblurring," in *The IEEE Conference on Computer Vision and Pattern Recognition (CVPR)*, June 2019.
- [17] O. Kupyn, V. Budzan, M. Mykhailych, D. Mishkin, and J. Matas, "Deblurgan: Blind motion deblurring using conditional adversarial networks," in *Proceedings of the IEEE conference on computer vision and pattern recognition*, 2018, pp. 8183–8192.
- [18] O. Kupyn, T. Martyniuk, J. Wu, and Z. Wang, "Deblurgan-v2: Deblurring (orders-of-magnitude) faster and better," in *Proceedings of the IEEE International Conference on Computer Vision*, 2019, pp. 8878–8887.
- [19] K. Zhang, W. Luo, Y. Zhong, L. Ma, B. Stenger, W. Liu, and H. Li, "Deblurring by realistic blurring," in *Proceedings of the IEEE/CVF Conference on Computer Vision and Pattern Recognition*, 2020, pp. 2737–2746.
- [20] P. Tran, A. Tran, Q. Phung, and M. Hoai, "Explore image deblurring via encoded blur kernel space," in *Proceedings of the IEEE Conference on Computer Vision and Pattern Recognition (CVPR)*, 2021.
- [21] R. Köhler, M. Hirsch, B. Mohler, B. Schölkopf, and S. Harmeling, "Recording and playback of camera shake: Benchmarking blind deconvolution with a real-world database," in *European conference on computer vision*. Springer, 2012, pp. 27–40.
- [22] W.-S. Lai, J.-B. Huang, Z. Hu, N. Ahuja, and M.-H. Yang, "A comparative study for single image blind deblurring," in *Proceedings of the IEEE Conference on Computer Vision and Pattern Recog.*, 2016, pp. 1701–1709.
- [23] Y.-W. Tai, X. Chen, S. Kim, S. J. Kim, F. Li, J. Yang, J. Yu, Y. Matsushita, and M. S. Brown, "Nonlinear camera response functions and image deblurring: Theoretical analysis and practice," *IEEE transactions on pattern analysis and machine intelligence*, vol. 35, no. 10, pp. 2498–2512, 2013.
- [24] A. Chakrabarti, "A neural approach to blind motion deblurring," in *European conference on computer vision*. Springer, 2016, pp. 221–235.
- [25] M. Delbracio and G. Sapiro, "Removing camera shake via weighted fourier burst accumulation," *IEEE Transactions on Image Processing*, vol. 24, no. 11, pp. 3293–3307, 2015.
- [26] F. Gavant, L. Alacoque, A. Dupret, and D. David, "A physiological camera shake model for image stabilization systems," in *SENSORS*, 2011 IEEE, 2014, pp. 1461–1464.
- [27] U. Schmidt, J. Jancsary, S. Nowozin, S. Roth, and C. Rother, "Cascades of regression tree fields for image restoration," *IEEE transactions on pattern analysis and machine intelligence*, vol. 38, no. 4, pp. 677–689, 2015.
- [28] A. Kuznetsova, H. Rom, N. Alldrin, J. Uijlings, I. Krasin, J. Pont-Tuset, S. Kamali, S. Popov, M. Mallocci, A. Kolesnikov *et al.*, "The open images dataset v4," *International Journal of Computer Vision*, vol. 128, no. 7, pp. 1956–1981, 2020.
- [29] D. Martin, C. Fowlkes, D. Tal, and J. Malik, "A database of human segmented natural images and its application to evaluating segmentation algorithms and measuring ecological statistics," in *Proceedings Eighth IEEE International Conference on Computer Vision. ICCV 2001*, vol. 2. IEEE, 2001, pp. 416–423.
- [30] C. J. Schuler, M. Hirsch, S. Harmeling, and B. Schölkopf, "Learning to deblur," *IEEE transactions on pattern analysis and machine intelligence*, vol. 38, no. 7, pp. 1439–1451, 2015.
- [31] J. Deng, W. Dong, R. Socher, L.-J. Li, K. Li, and L. Fei-Fei, "Imagenet: A large-scale hierarchical image database," in *2009 IEEE conference on computer vision and pattern recognition*. IEEE, 2009, pp. 248–255.
- [32] T.-Y. Lin, M. Maire, S. Belongie, J. Hays, P. Perona, D. Ramanan, P. Dollár, and C. L. Zitnick, "Microsoft coco: Common objects in context," in *European conference on computer vision*. Springer, 2014, pp. 740–755.
- [33] B. Zhou, H. Zhao, X. Puig, S. Fidler, A. Barriuso, and A. Torralba, "Scene parsing through ade20k dataset," in *Proceedings of the IEEE Conference on Computer Vision and Pattern Recognition*, 2017.
- [34] S. W. Hasinoff and K. N. Kutulakos, "A layer-based restoration framework for variable-aperture photography," in *IEEE 11th International Conference on Computer Vision, ICCV 2007, Rio de Janeiro, Brazil, October 14-20, 2007*. IEEE Computer Society, 2007, pp. 1–8. [Online]. Available: <https://doi.org/10.1109/ICCV.2007.4408898>

## APPENDIX

A. Noise and  $\gamma$ -correction

The effect of modeling  $\gamma$ -correction and adding noise is shown in Figure 8 for images from the Kohler dataset. This dataset assumes a linear camera response function, and therefore better results are achieved when training with datasets that do not account for  $\gamma$ -correction. We call  $N$ - $SBDD$  and  $N$ - $SBDD(\gamma)$  to the models obtained by adding Gaussian noise with a standard deviation equal to 0.02 to the blurry images during training. The noise added during training generates a cartoon effect on the deblurred images, similar to the case of the *Total Variation* prior. In some cases, it helps to better recover the structure of the image at the expense of missing fine details. Quantitative results are shown in Tab. IV.

TABLE IV

QUANTITATIVE EVALUATION ON REAL DATASETS FOR THE SRN [15] MODELS TRAINED WITH AND WITHOUT ADDITIVE NOISE.  $SBDD$ : NO  $\gamma$ -CORRECTION, NO ADDITIVE NOISE.  $N$ - $SBDD$ : NO  $\gamma$ -CORRECTION, ADDITIVE GAUSSIAN NOISE.  $SBDD(\gamma)$ :  $\gamma$ -CORRECTION, NO ADDITIVE NOISE.  $N$ - $SBDD(\gamma)$ :  $\gamma$ -CORRECTION, ADDITIVE GAUSSIAN NOISE.

Training Set	Test Sets	
	RealBlur	Kohler
$SBDD$	29.65/ 0.897	29.01/ 0.828
$N$ - $SBDD$	29.39/ 0.885	28.36/ 0.811
$SBDD(\gamma)$	29.94/ 0.898	27.70/ 0.812
$N$ - $SBDD(\gamma)$	29.84/ 0.888	27.37/ 0.802

## B. Restoring in the Space of Photons

The experimental results shown in the article together with the results above highlight the importance of  $\gamma$ -correction in deblurring methods performance. In the experiment presented in this section, we trained an SRN model to restore in the space of photons instead of the pixels' space. To this end, we inverted the  $\gamma$ -correction step before feeding the network with the blurry image. Then, the output of the network is  $\gamma$ -corrected before computing the *loss*. Results on real images (Tab. V) and on synthetic datasets (Tab. VI) are similar to those obtained in the space of pixels with the appropriate training set. The main advantage of this procedure is that it is possible to decide in inference time whether to apply  $\gamma$ -correction or not. The same model can be used effectively with a wider set of images.

TABLE V

SRN [15] RESULTS WITH REAL DATASETS WHEN TRAINING IN THE SPACE OF PHOTONS. BLURRY IMAGES WERE GENERATED USING THE SAME PROCEDURE DESCRIBED IN THE MANUSCRIPT.

Training Set	Test Sets	
	RealBlur	Köhler
Photons ( $\gamma = 1$ )	29.83/ 0.896	28.89/ 0.824
SRN + $SBDD$	29.65/ 0.897	29.01/ 0.828
Photons ( $\gamma = 2.2$ )	29.85/ 0.888	27.64/ 0.811
SRN + $SBDD(\gamma)$	29.94/ 0.898	27.70/ 0.812

## C. Results using DeepDeblur Architecture [5]

Fig. 9 and Fig. 10 compare the results obtained by different DeepDeblur [5] models on real images from Lai's dataset [22].

We compare the models provided by the authors with a model trained on the proposed  $SBDD(\gamma)$  dataset. The model was trained during 200 epochs using the default parameters.

## D. Comparison on the RealBlur Dataset [8]

Tab. II shows that training using  $SBDD$  gives the best cross-dataset performance in the RealBlur dataset [8]. In Fig. 11 we compare a model trained on  $SBDD$  versus a model trained on RealBlur on images from the RealBlur test set. The main differences observed are slight changes in general lighting and that our restorations appear brighter in saturated areas.

## E. Uniform vs Non-uniform Blur

The synthetic non-uniform dataset of Lai *et al.* [22] is useful to show the capacity of networks trained with the uniformly blurred dataset to deal with non-uniform situations. Quantitative results were presented in Sec. IV-C, along with qualitative results. Here we show several additional examples for different motion blur fields of the dataset, depicted in Figures 12, 13, 14 and 15. Best results are obtained with SRN trained on the proposed  $SBDD$  dataset and very close is SRN trained on BSD-B [8]. SRN trained on GoPro and RealBlur does not obtain good results, despite having non-uniformly blurred images in the dataset.

## F. Results in RWBI Dataset [19]

Results are shown in Fig. 16.

## G. Results in Lai Dataset [22]

Results are shown in Fig. 17.

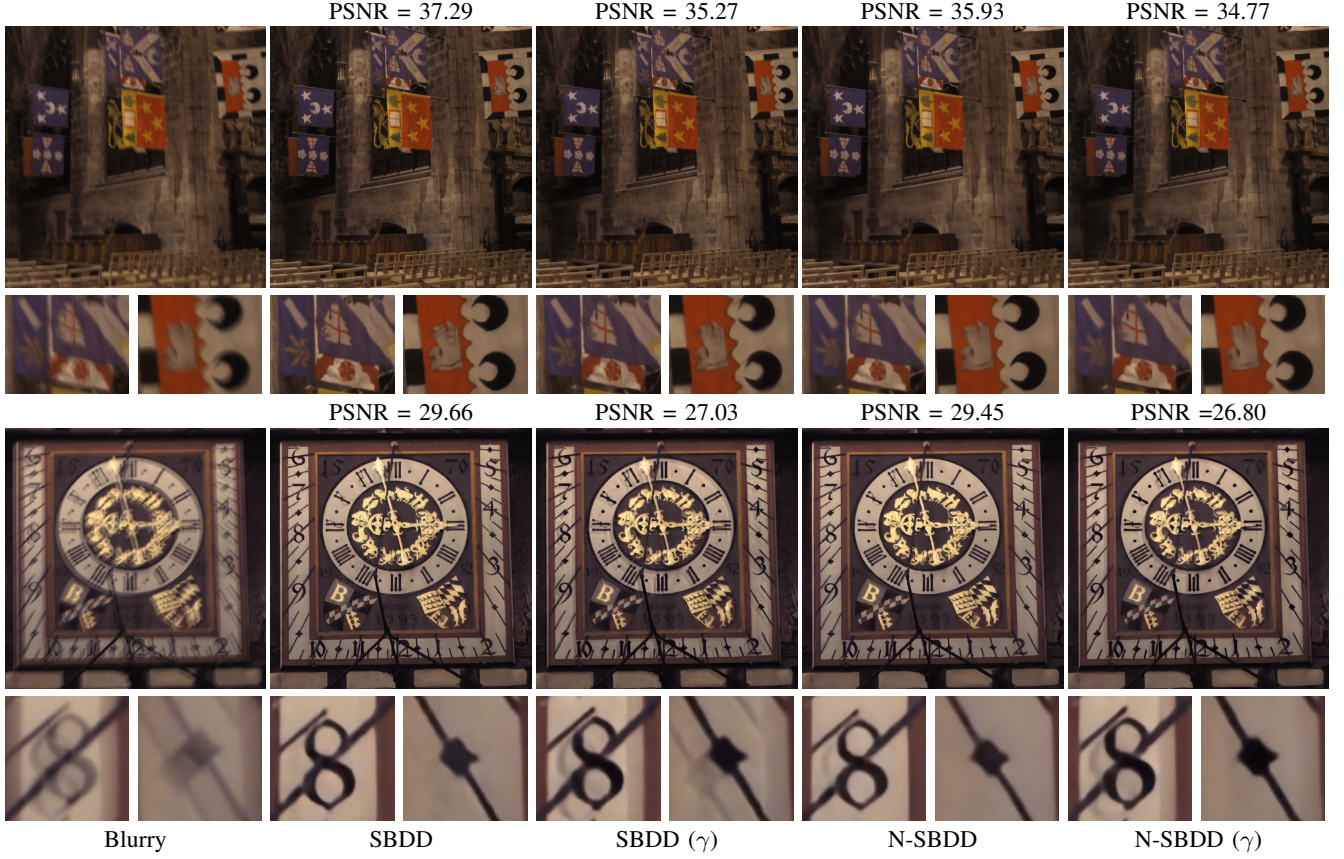
Fig. 8. Effect of noise and  $\gamma$ -correction

TABLE VI

SRN RESULTS WITH SYNTHETIC DATASETS WHEN TRAINING ON THE PROPOSED DATASET IN THE SPACE OF THE PHOTONS. A SINGLE MODEL TRAINED IN THE PHOTONS' SPACE CAN BE EFFECTIVELY USED TO RESTORE IMAGES AFFECTED BY LINEAR (GoPro, Lai, DVD)) AND NON-LINEAR (GoPro( $\gamma$ , REDS)) CAMERA RESPONSE FUNCTIONS. SETTING THE  $\gamma$ -VALUE AT INFERENCE TIME PRODUCES SIMILAR RESULTS TO MODELS TRAINED ON DATASETS SYNTHESIZED WITH THE APPROPRIATE CAMERA RESPONSE FUNCTION.

Training Sets	Test Sets				
	GoPro	GoPro( $\gamma$ )	REDS	Lai (NU)	DVD
Photons ( $\gamma = 1$ )	29.68/ 0.894	28.41/ 0.883	27.06/ 0.827	22.52/ 0.738	29.43/ 0.883
SBDD	29.61/ 0.895	28.15/ 0.880	26.78/ 0.822	22.83/ 0.740	29.40/ 0.882
Photons ( $\gamma = 2.2$ )	28.03/ 0.881	29.62/ 0.896	28.96/ 0.858	21.0 / 0.687	28.23/ 0.870
SBDD ( $\gamma$ )	28.13/ 0.873	29.56/ 0.896	29.04/ 0.860	21.08/ 0.694	28.23/ 0.870

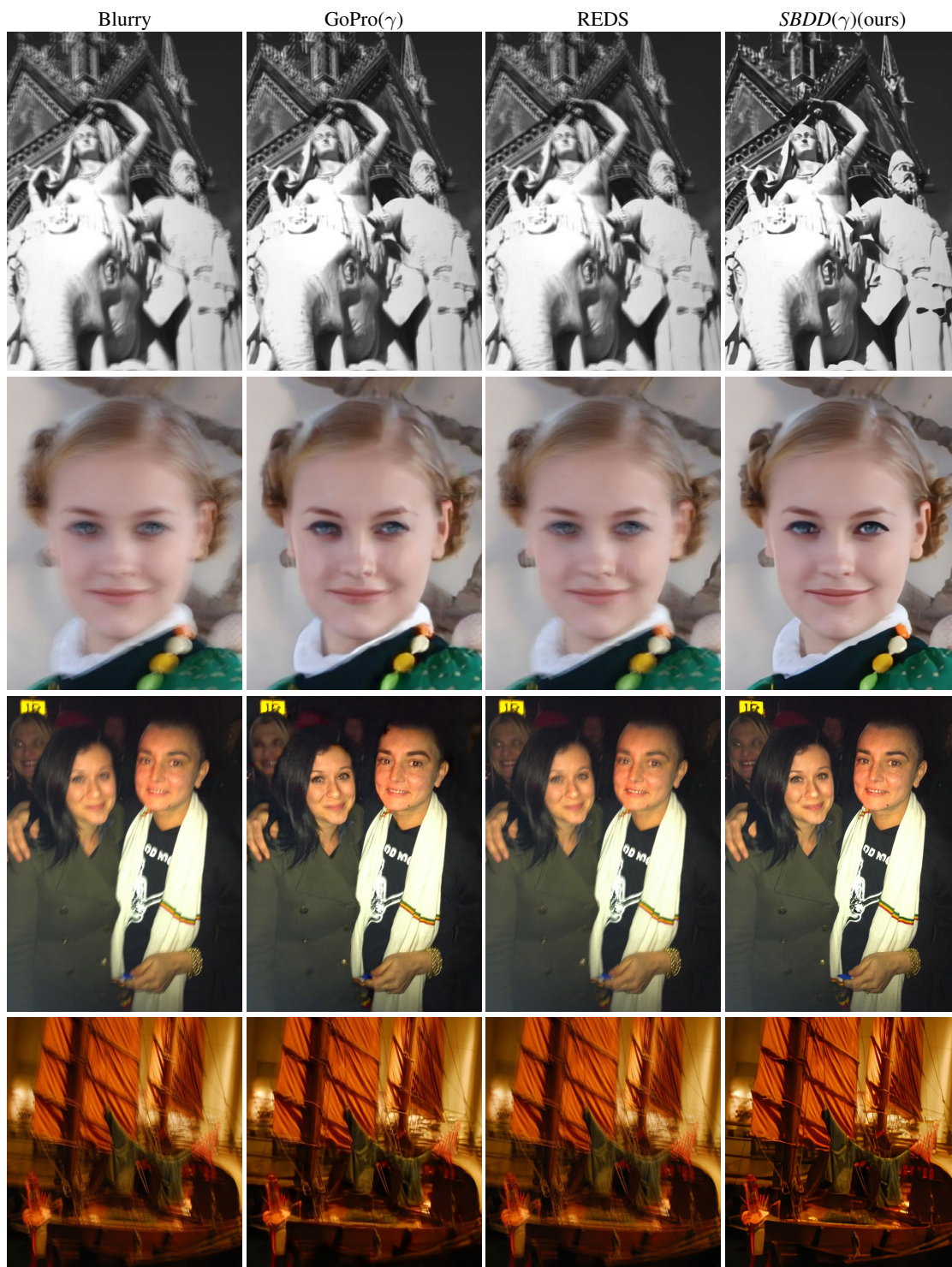


Fig. 9. Effect of the training set on the DeepDeblur architecture [5]. Results on real images improve when DeepDeblur is trained on the proposed *SBDD* dataset.

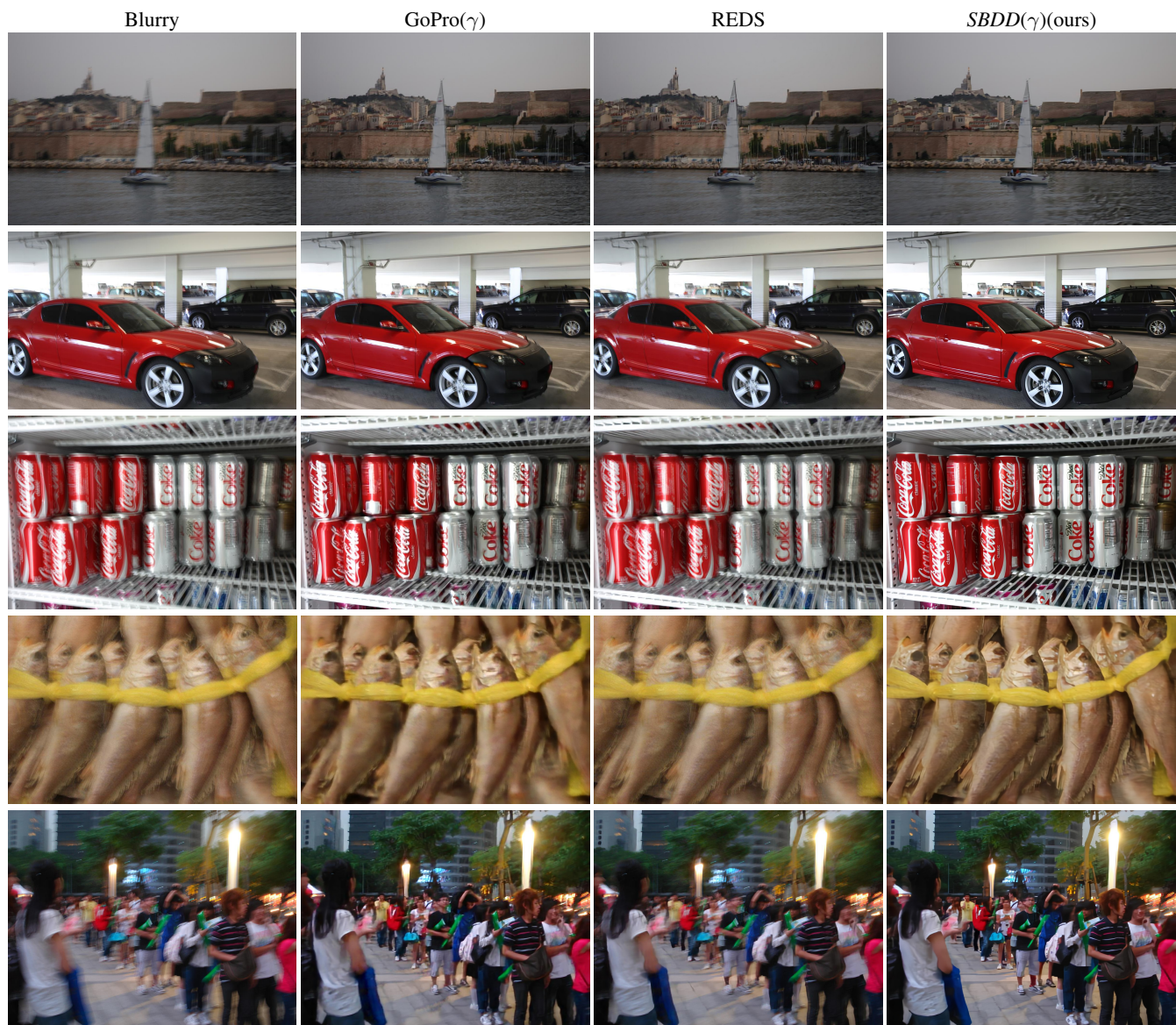


Fig. 10. Effect of the training set on the DeepDeblur architecture [5]. Results on real images improve when DeepDeblur is trained on the proposed *SBDD* dataset.



Fig. 11. Results of training SRN [15] on *SBDD* vs training SRN [15] on *RealBlur* [8]. Our cross-domain results are comparable to the model trained with *RealBlur* in the *RealBlur* test set.

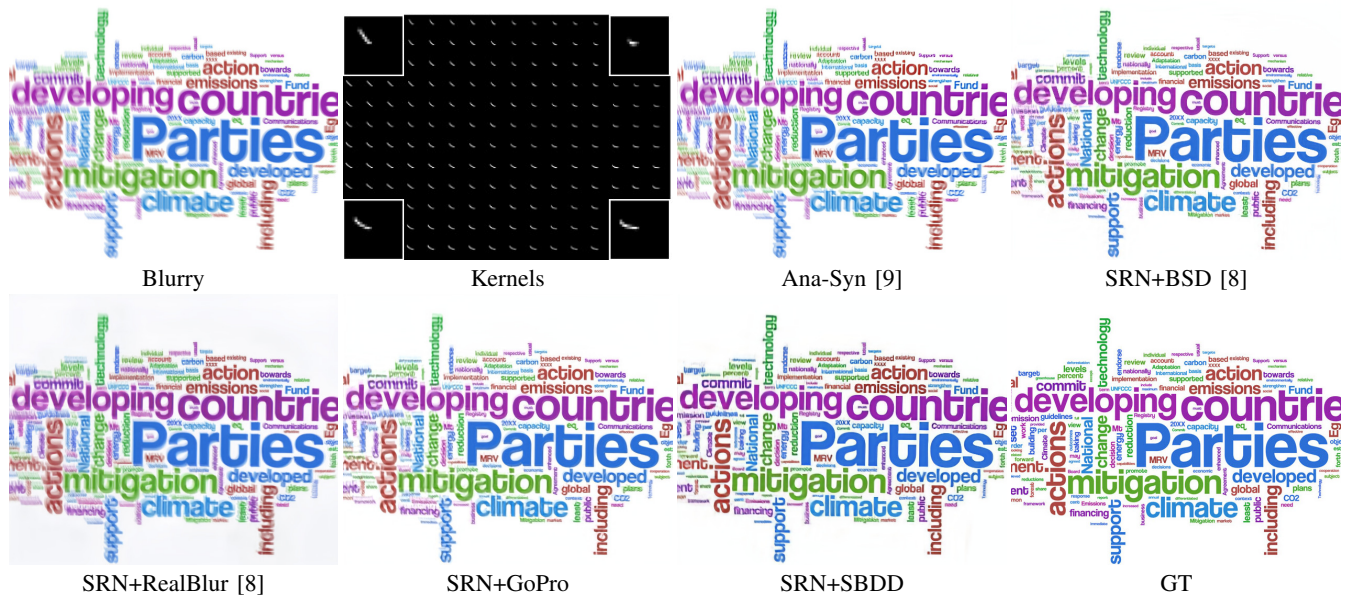


Fig. 12. Comparison of results on a non-uniformly blurred image from the synthetic Lai dataset. The Blurry image was generated from the GT. The motion blur kernels are shown in the second image from the first row.

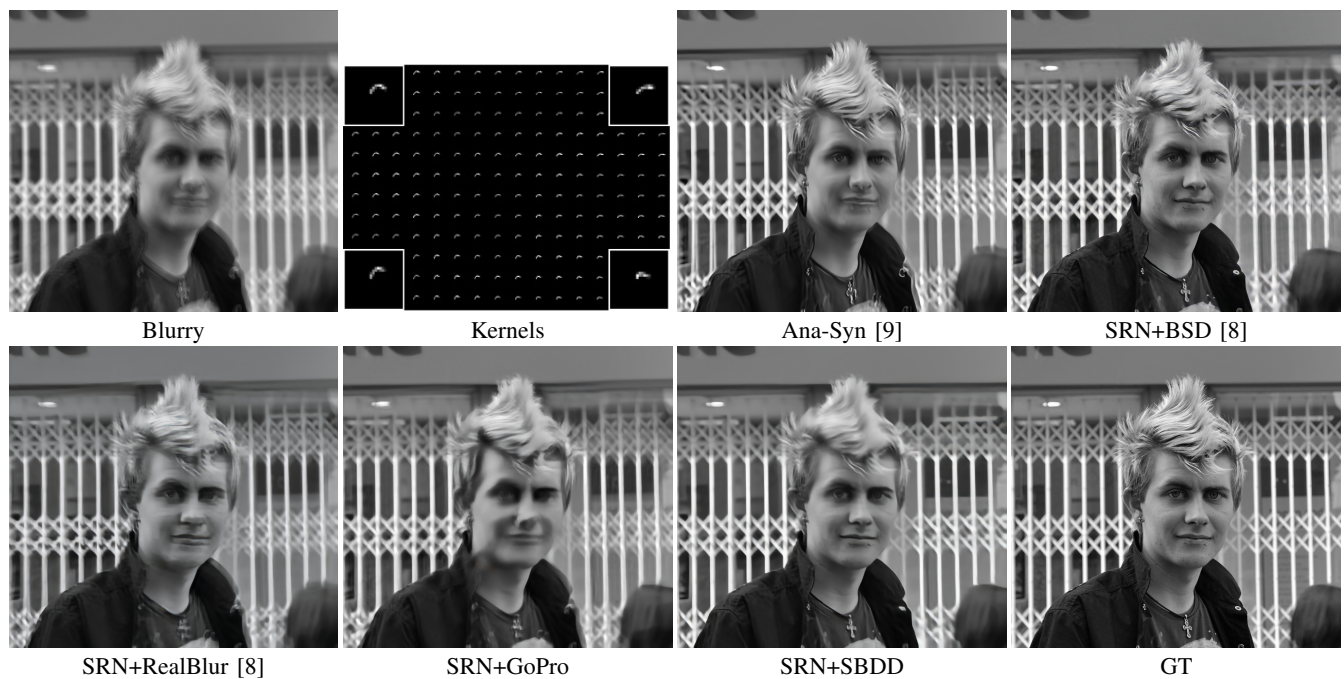


Fig. 13. Comparison of results on a non-uniformly blurred image from the synthetic Lai dataset. The Blurry image was generated from the GT. The motion blur kernels are shown in Kernels.

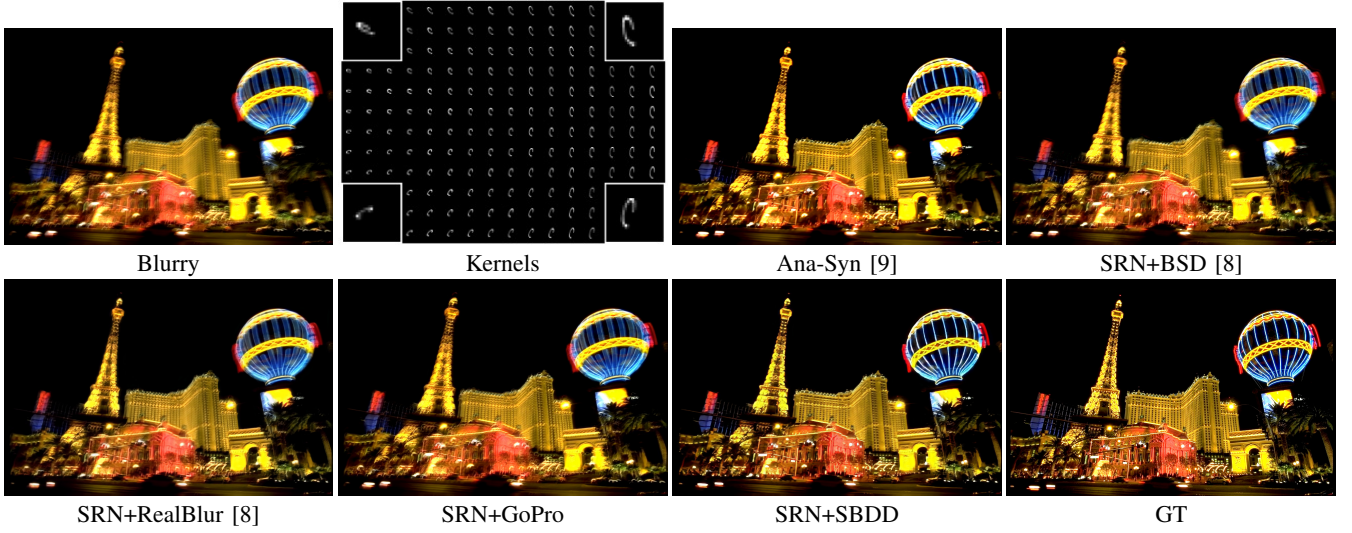


Fig. 14. Comparison of results on a non-uniformly blurred image from the synthetic Lai dataset. The Blurry image was generated from the GT. The motion blur kernels are shown in the second image from the first row.

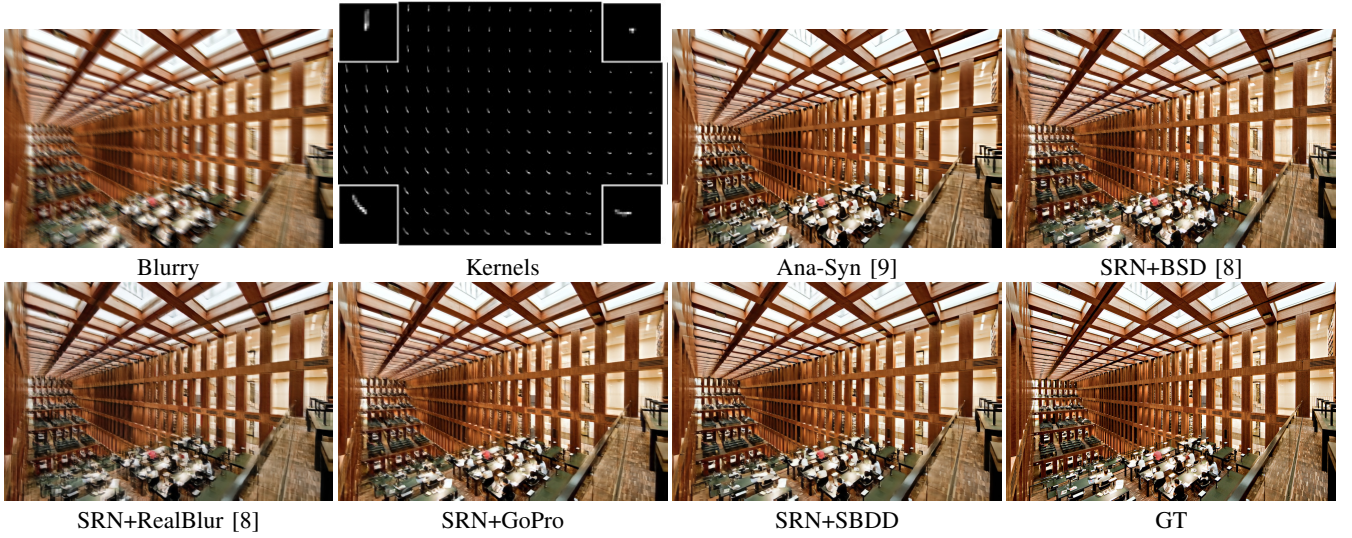


Fig. 15. Comparison of results on a non-uniformly blurred image from the synthetic Lai dataset. The Blurry image was generated from the GT. The motion blur kernels are shown in the second image from the first row.

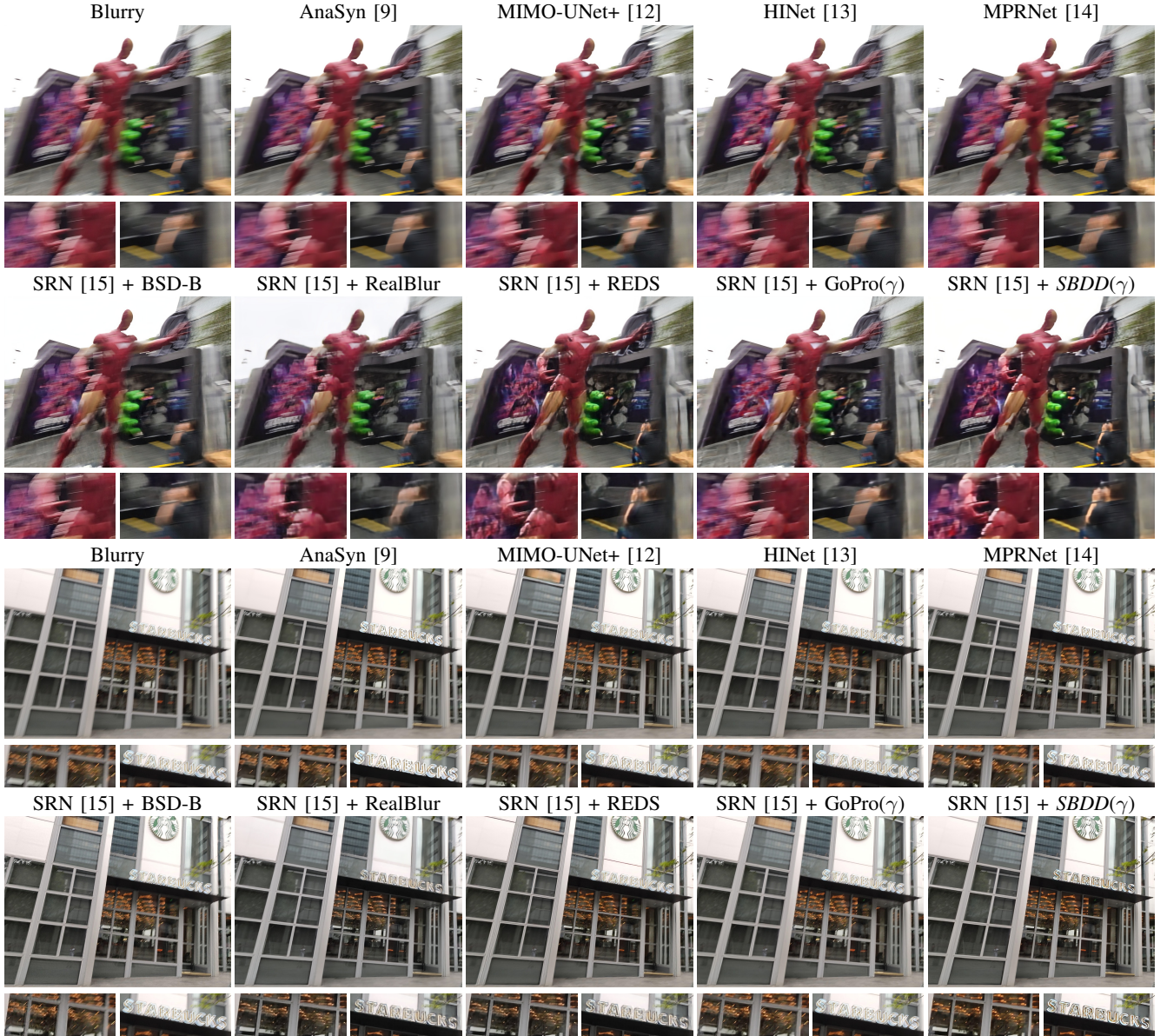


Fig. 16. Comparison on recent deep deblur methods on the Real-World Blurred Image (RWBI) dataset [19] of images with real blur.



Fig. 17. Comparison to recent deep deblur methods on the Lai dataset [22] of images with real blur.